PHYSICAL REVIEW B **84**, 205441 (2011)

Electronic and optical properties of a circular graphene quantum dot in a magnetic field: Influence of the boundary conditions

M. Grujić,[1,*] M. Zarenia,[2,†] A. Chaves,[3,‡] M. Tadić,[1,§] G. A. Farias,[3,‖] and F. M. Peeters[2,3,¶]
[1]*School of Electrical Engineering, University of Belgrade, P.O. Box 3554, 11120 Belgrade, Serbia*
[2]*Department of Physics, University of Antwerp, Groenenborgerlaan 171, B-2020 Antwerp, Belgium*
[3]*Departamento de Física, Universidade Federal do Ceará, Caixa Postal 6030, Campus do Pici, 60455-900 Fortaleza, Ceará, Brazil*

(Received 7 July 2011; revised manuscript received 27 October 2011; published 21 November 2011)

An analytical approach, using the Dirac-Weyl equation, is implemented to obtain the energy spectrum and optical absorption of a circular graphene quantum dot in the presence of an external magnetic field. Results are obtained for the *infinite-mass* and *zigzag* boundary conditions. We found that the energy spectrum of a dot with the zigzag boundary condition exhibits a zero-energy band regardless of the value of the magnetic field, while for the infinite-mass boundary condition, the zero-energy states appear only for high magnetic fields. The analytical results are compared to those obtained from the tight-binding model: (i) we show the validity range of the continuum model and (ii) we find that the continuum model with the infinite-mass boundary condition describes rather well its tight-binding analog, which can be partially attributed to the blurring of the mixed edges by the staggered potential.

DOI: 10.1103/PhysRevB.84.205441 PACS number(s): 71.10.Pm, 73.21.−b, 81.05.ue

I. INTRODUCTION

Graphene is an allotrope of carbon that, due to its novel properties, has attracted considerable attention recently.[1,2] The energy spectrum of graphene is linear at two inequivalent points (K and K') in the Brillouin zone. Such a linear behavior is a characteristic of relativistic massless particles, which can be described by the Dirac-Weyl equation.[3] Due to the well-known Klein tunneling effect,[4] which prevents carrier confinement, manufacturing graphene-based quantum structures is a big challenge for future applications in electronic devices. However, the energy of charge-carrier states in graphene can be manipulated either by using external magnetic fields, which leads to the appearance of Landau levels for an infinite graphene sheet, or by using finite-size graphene quantum dots (GQD's).[5]

The energy levels of circular graphene dots in the presence of a perpendicular magnetic field were recently investigated analytically in Ref. 6 for the special case of the infinite-mass boundary condition (IMBC). On the other hand, it was recently shown that the electron and hole states in graphene nanostructures depend sensitively on the edge topology. For instance, for a zigzag termination in graphene nanoribbons and graphene flakes, such as triangular and hexagonal GQD's, a band of zero-energy edge-localized states is found.[7–9] Except for the case in which all the edges of the graphene flake are armchair, the appearance of the zero-energy states seems to be robust with respect to edge roughness, as demonstrated by the persistent finite density of these states observed in realistic quasicircular GQD's.[10]

It has been shown that graphene structures with zigzag segments on the edge having zero-energy states are prone to spontaneous magnetic ordering[11] when electron-electron interaction is included. This many-particle interaction leads to a small energy gap. In such systems, spin polarization is found in zigzag-edge-dominated GQD's.[12] In the presence of an IMBC, the single-particle energy spectrum of a GQD exhibits already a gap around zero energy for low magnetic fields.[6] Thus in this case no magnetic ordering is expected. Therefore, it is important to determine what notable differences in the energy spectra may arise from the application of different boundary conditions. Furthermore, because of the possible applications of the GQD's for light detection and solar energy conversion,[13] it is interesting to explore how the choice of the boundary condition affects the absorption spectrum.

In this paper, we analytically solve the Dirac-Weyl equation for a circular graphene quantum dot in the presence of a perpendicular magnetic field for both infinite-mass and zigzag boundary conditions. A comparison between the energy spectra and angular current densities obtained for each boundary condition is made. In addition to the exact solutions, we also present analytic expressions where the magnetic field is treated as a perturbation, which agrees well with the exact solution for small fields. Further, we discuss the effect of a magnetic field on the optical spectrum of a circular GQD, where we analyze the effect of different boundary conditions (i.e., ZZBC and IMBC) on the interband optical transitions.

To validate the continuum model, we present here also the results obtained within the tight-binding (TB) model, where there is no ambiguity as far as the boundary conditions are concerned.[14] We compare the analytical spectra obtained by the Dirac-Weyl equation to those obtained by the TB model for circular dots. Two kinds of dots are considered in the TB model: (i) a circular dot cut out from a graphene honeycomb lattice, and (ii) a circular confinement region delimited by an infinite-mass barrier. The former case has an admixture of zigzag and armchair edges, and, due to the zigzag parts, a band of quasi-zero-energy levels is found. In the latter case, no zero-energy states are present. We critically examine how the continuum model results compare to the TB results, and which microscopical details in the latter are not captured by the approximations made in the former.

The paper is organized as follows. We present the analytical results (i.e., energy spectrum, current density, and optical absorption spectra) based on the continuum model in Sec. II. The results obtained from the TB model are given in Sec. III.

The paper is concluded in Sec. IV. In the Appendix, details of the calculations for the approximate energy levels in small magnetic fields (using perturbation theory) are presented.

II. THE CONTINUUM APPROACH

The Dirac-Weyl Hamiltonian for low-energy electron states in graphene, in the presence of a perpendicular magnetic field and a mass-related potential, reads

$$H = v_F(\mathbf{p} + e\mathbf{A}) \cdot \boldsymbol{\sigma} + V(r)\sigma_z. \tag{1}$$

Here $\boldsymbol{A} = (0, B\rho/2, 0)$ is the vector potential in symmetric gauge and $\boldsymbol{\sigma}$ denotes the Pauli matrices, which takes into account contributions of two different graphene sublattices. This equation holds for the K valley states, and $\boldsymbol{\sigma}$ in this equation should be replaced by its complex conjugate $\boldsymbol{\sigma}^*$ when considering states in the K' valley. We assume that the carriers are confined in a circular area of radius R, which is modeled by an infinite mass outside the dot, i.e., $V(r) = 0$ for $r < R$ and $V(r) \to \infty$ for $r \geqslant R$, where r is the radial coordinate of the cylindrical coordinates system. In the case of the adopted ZZBC, the two Dirac cones are labeled by the quantum number k, which has the value $+1$ in the K valley and -1 in the K' valley. For the IMBC, however, we use the so called valley-isotropic form of the Hamiltonian, with fixed $k = +1$, and the valleys are differentiated by another quantum number τ, which appears in the boundary condition itself.[15] Furthermore, we introduce the dimensionless variables $\rho = r/R$, $\beta = R^2/2l_B^2 = eBR^2/2\hbar$, and $\varepsilon = E/E_0 = ER/\hbar v_F$, where E is the carrier energy, v_F is the Fermi velocity, and $l_B = \sqrt{\hbar/eB}$ is the magnetic length. The Dirac equation (1) in these dimensionless units reduces to the form

$$\begin{bmatrix} 0 & \pi_- \\ \pi_+ & 0 \end{bmatrix} \begin{bmatrix} \psi_1(\rho,\phi) \\ \psi_2(\rho,\phi) \end{bmatrix} = \varepsilon \begin{bmatrix} \psi_1(\rho,\phi) \\ \psi_2(\rho,\phi) \end{bmatrix}, \tag{2}$$

where $\pi_\pm = -ie^{\pm ik\phi}[\partial_\rho \pm \frac{ik}{\rho}\partial_\phi \mp k\beta\rho]$. Because of the coupling between the orbital angular momentum L_z and pseudospin $\hbar\sigma_z/2$, we define the total momentum $J_z = L_z + \hbar\sigma_z/2$. We have $[H, J_z] = 0$, i.e., the total angular momentum is a conserved quantity, and thus the two-component wave function has the form

$$\psi(\rho,\phi) = e^{im\phi} \begin{pmatrix} \chi_1(\rho) \\ e^{ik\phi}\chi_2(\rho) \end{pmatrix}, \tag{3}$$

where $m = 0, \pm 1, \pm 2, \ldots$ is the total angular momentum quantum number. The two components of the wave function correspond to different sublattices, i.e., χ_1 corresponds to the sublattice A and χ_2 corresponds to the sublattice B.

Equation (2) is solved with the boundary condition that expresses that the outward current at the graphene edge is zero. This leads to the following relation at the dot edge:[16]

$$\tan(\phi) = -\mathrm{Re}[\psi_1^*(1,\phi)\psi_2(1,\phi)]/\mathrm{Im}[\psi_1^*(1,\phi)\psi_2(1,\phi)], \tag{4}$$

where Re (Im) is the real (imaginary) part. The two boundary conditions

$$\frac{\psi_2(1,\phi)}{\psi_1(1,\phi)} = i\tau e^{i\phi} \to \frac{\chi_2(1)}{\chi_1(1)} = i\tau, \tag{5a}$$

$$\psi_1(1,\phi) = 0 \to \chi_1(1) = 0, \tag{5b}$$

both satisfy Eq. (4). The condition given by Eq. (5a) is called the infinite-mass boundary condition (IMBC)[16] and imposes the requirement that the region outside the dot is forbidden for particles due to the relationship $v_F \propto 1/m$, as demonstrated in Ref. 17. $\tau = +1(-1)$ is used for the $K(K')$ states. The condition Eq. (5b) requires that one of the wave-function components is zero at the dot edge, which is called the zigzag boundary condition (ZZBC).[18] Note that a graphene quantum dot with circular geometry in principle includes both armchair and zigzag edges at the boundary, which will be considered in Sec. III within the TBM model. Here, within the continuum model, we consider for definiteness only ZZBC at the edges. In the case of armchair edges, the boundary condition includes the wave spinors corresponding to both K and K' points, which is given by

$$\psi_1^K e^{i\boldsymbol{K}\cdot\boldsymbol{r}} + \psi_1^{K'} e^{i\boldsymbol{K}'\cdot\boldsymbol{r}} = \mathbf{0}, \tag{6a}$$

$$\psi_2^K e^{i\boldsymbol{K}\cdot\boldsymbol{r}} + \psi_2^{K'} e^{i\boldsymbol{K}'\cdot\boldsymbol{r}} = \mathbf{0}. \tag{6b}$$

In addition to k and τ, we show below that the states in the analyzed circular GQD are labeled by the total angular quantum number m and the principal quantum number n. Therefore, it is convenient to denote them by the symbol (m,n). The symbol n is also identified as the Landau level number. In discussing the various properties of the spectrum in the continuum model, we use the notation $\varepsilon_{k,m,n}^p$, where $p \in e$ (h) denotes electron (hole) eigenvalues, k is the valley index, and it is equal to k or τ when considering the ZZBC or IMBC spectrum, respectively. Furthermore, n is omitted in zero-field discussions.

A. Zero-energy solutions

When $\varepsilon = 0$, the differential equations (2) are decoupled,

$$\frac{d\chi_1(\rho)}{d\rho} - \frac{mk}{\rho}\chi_1(\rho) - k\beta\rho\chi_1(\rho) = 0, \tag{7a}$$

$$\frac{d\chi_2(\rho)}{d\rho} + \frac{(mk+1)}{\rho}\chi_2(\rho) + k\beta\rho\chi_2(\rho) = 0. \tag{7b}$$

which offers straightforward solutions of the form $\chi_1(\rho) = C_1\rho^{mk}e^{k\beta\rho^2/2}$ and $\chi_2(\rho) = C_2\rho^{-(mk+1)}e^{-k\beta\rho^2/2}$.

These solutions cannot simultaneously satisfy the IMBC of Eq. (5a) and be normalizable. Namely, if the normalization condition is imposed, either C_1 or C_2, depending on the sign of m, should vanish, which prevents Eq. (5a) from being satisfied. Thus, we conclude that there are no zero-energy states in the IMBC spectrum.

If the ZZBC, Eq. (5b), is employed, it is possible to find normalizable zero-energy solutions in both valleys. Those solutions are constructed by assuming $C_1 = 0$ and $C_2 \neq 0$ for both the $m < 0$ states in the K valley and the $m > 0$ states in the K' valley. Therefore, adopting ZZBC allows the appearance of a zero-energy band. Those wave-function components have the form $\chi_1(\rho) = 0$ and $\chi_2(\rho) = C\rho^{-(mk+1)}e^{-k\beta\rho^2/2}$, with $mk = -1, -2, -3, \ldots$. Obviously, these states are completely pseudo-spin-polarized and reside on the B sublattice sites. The form of the wave function indicates that all states, except $mk = -1$, are edge-localized, as is expected for zero-energy zigzag states. Furthermore, states with larger $|m|$ are localized closer to the edge.

B. Nonzero-energy solutions for $\beta = 0$

When $\varepsilon \neq 0$ and when the magnetic field is zero, i.e., $\beta = 0$, Eqs. (2) are coupled. Substitution of χ_2 from the second into the first differential equation leads to the Bessel differential equation

$$\rho^2 \frac{d^2\chi_1(\rho)}{d\rho^2} + \rho \frac{d\chi_1(\rho)}{d\rho} + (\varepsilon^2\rho^2 - m^2)\chi_1(\rho) = 0, \tag{8}$$

with the solution

$$\chi_1(\rho) = C_1 J_m(\varepsilon\rho). \tag{9}$$

From Eq. (2), the relation between the first and second component of the wave function follows,

$$\psi_2(\rho,\phi) = \frac{e^{ik\phi}}{\varepsilon}\left(-i\partial_\rho + \frac{k}{\rho}\partial_\phi + ik\beta\rho\right)\psi_1(\rho,\phi), \tag{10}$$

and thus

$$\chi_2(\rho) = ikC_1 J_{m+k}(\varepsilon\rho). \tag{11}$$

The boundary condition (5a) leads to the equation $\tau J_m(\varepsilon) = J_{m+1}(\varepsilon)$, while the boundary condition (5b) gives $J_m(\varepsilon) = 0$. Recalling that the Bessel functions obey the properties $J_m(\varepsilon) = (-1)^m J_{-m}(\varepsilon)$ and $J_m(\varepsilon) = (-1)^m J_m(-\varepsilon)$, several interesting properties of the zero-field energy spectra are derived: (i) There is electron-hole symmetry in both valleys for ZZBC, which is reflected via the expression $\varepsilon^e_{\pm1,m} = -\varepsilon^h_{\pm1,m}$. Unlike ZZBC, IMBC is known to break electron-hole symmetry,[18] so the former relations do not hold. However, there is a similar symmetry property for IMBC, for which the expression $\varepsilon^e_{\pm1,m} = -\varepsilon^h_{\pm1,-(m+1)}$ holds. (ii) Intervalley spectrum symmetry is present for ZZBC, $\varepsilon^{e,h}_{+1,m} = \varepsilon^{e,h}_{-1,m}$, whereas for IMBC, $\varepsilon^{e,h}_{+1,m} = \varepsilon^{e,h}_{-1,-(m+1)}$. The latter two properties for IMBC further indicate intervalley electron-hole symmetry between states of the same m, i.e., $\varepsilon^e_{\pm1,m} = -\varepsilon^h_{\mp1,m}$. (iii) Finally, we may deduce that the energy spectrum within each valley is either doubly degenerate (for $m \neq 0$, $\varepsilon^{e,h}_{\pm1,+m} = \varepsilon^{e,h}_{\pm1,-m}$) or nondegenerate (for $m = 0$) if ZZBC is adopted, whereas this is not the case for IMBC.

C. Nonzero energy solutions for $\beta \neq 0$

For the general case $\varepsilon \neq 0$ and $\beta \neq 0$, we obtain the differential equation for χ_1,

$$\left(\frac{d^2}{d\rho^2} + \frac{1}{\rho}\frac{d}{d\rho} - \left[2\beta(m+k) + \frac{m^2}{\rho^2} + \beta^2\rho^2 - \varepsilon^2\right]\right)\chi_1(\rho) = 0, \tag{12}$$

where the symmetric gauge is used for the magnetic field. This equation has the normalizable solution

$$\psi_1(\rho,\phi) = Ce^{im\phi}\rho^m e^{-\beta\rho^2/2} \times {}_1\widetilde{F}_1\left(\frac{2m+k+1}{2} - \frac{\varepsilon^2}{4\beta}, m+1, \beta\rho^2\right), \tag{13}$$

where we used the relation $\psi_1(\rho,\phi) = e^{im\phi}\chi_1(\rho)$, obtained from Eqs. (2) and (3), and ${}_1\widetilde{F}_1(a,b,z)$ is the regularized confluent hypergeometric function. The second component of the wave function is extracted from Eq. (10), and for the $K(k=1)$ and $K'(k=-1)$ valleys it reads

$$\psi_2(\rho,\phi) = ikCe^{i(m+k)\phi}\frac{2\rho^{m+k}}{\varepsilon}\left[\frac{(1-k)}{2} + \frac{(1+k)}{2}\frac{\varepsilon^2}{4}\right] \times e^{-\beta\rho^2/2}{}_1\widetilde{F}_1\left(\frac{2m+k+1}{2} - \frac{\varepsilon^2}{4\beta}, m+k+1, \beta\rho^2\right). \tag{14}$$

The IMBC leads to the following eigenvalue equation:

$$\frac{\tau\varepsilon}{2}{}_1\widetilde{F}_1\left(m+1-\frac{\varepsilon^2}{4\beta}, m+2, \beta\right) - {}_1\widetilde{F}_1\left(m+1-\frac{\varepsilon^2}{4\beta}, m+1, \beta\right) = 0, \tag{15}$$

while for the ZZBC we obtain

$${}_1\widetilde{F}_1\left(\frac{2m+k+1}{2} - \frac{\varepsilon^2}{4\beta}, m+1, \beta\right) = 0. \tag{16}$$

From (15) and (16) we may deduce that for each BC the magnetic field breaks all but one symmetry property, which were stated in previous section. Thus from Eq. (15) one may notice that the energy levels of the K and K' valleys are symmetric as $\varepsilon^e_{\pm1,m} = -\varepsilon^h_{\mp1,m}$. On the other hand, when the ZZBC is adopted, Eq. (16) depends on ε^2, and consequently the electron and hole states in each valley are symmetric with respect to each other.

D. Energy spectrum

We now analyze the magnetic field dependence of the energy spectra in more detail. In Fig. 1, we show the energy levels of a circular dot with radius $R = 70$ nm and $-4 \leqslant m \leqslant 4$ for both the (a) IMBC and (b) ZZBC cases. The spectrum at the K valley is displayed by the solid blue curves, whereas the red dashed curves denote the energy levels in the K' valley. The zero-energy localized zigzag state (ZES) is shown by the horizontal solid black line in Fig. 1(b). Notice that IMBC leads to an energy gap in the spectrum, as is evident in Fig. 1(a). The lowest nonzero electron energy level in both IMBC and ZZBC initially decreases linearly with magnetic field (as is similar for semiconductor quantum dots) but then decreases as a Gaussian at high magnetic fields (which is different from the $1/\beta$ behavior found in semiconductor quantum dots). We fitted the energy level to a Gaussian function $\varepsilon(\beta) = a\exp\{-([\beta - b]/c)^2\}$ [see green solid curves in Figs. 1(a) and 1(b)], where $(a,b,c)_{\mathrm{IMBC}} = (3,-3.9,4.55)$ and $(a,b,c)_{\mathrm{ZZBC}} = (4.47,-7.1,9)$ are the fitting parameters, respectively, for the IMBC and ZZBC. We found a relation between the parameter c of the different energy levels: $c^i_{\mathrm{IMBC}} \approx 1.15c^{i-1}_{\mathrm{IMBC}}$ and $c^i_{\mathrm{ZZBC}} \approx c^{i-1}_{\mathrm{ZZBC}}$ (with i being the eigenstate index), respectively, for IMBC and ZZBC.

The magnetic ordering at the dot edge breaks reversal symmetry, and thus the electron-hole symmetry for each valley is broken, even when an external magnetic field is absent. Therefore, the energies of the electron and hole states in a given valley are not mutually related. However, the magnetic ordering cannot break the intervalley electron-hole

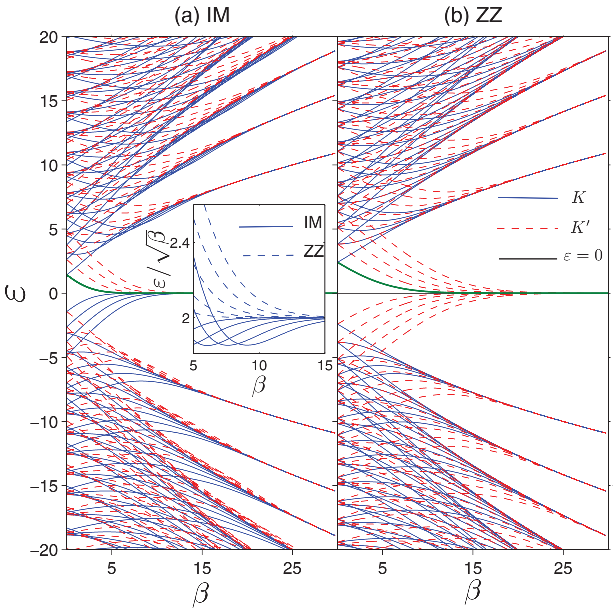

FIG. 1. (Color online) Energy spectrum of a circular graphene quantum dot with $R = 70$ nm in a perpendicular magnetic field for (a) IMBC and (b) ZZBC. The energy levels corresponding to the K and K' valleys are shown, respectively, by the blue solid curves and the red dashed curves. The zigzag zero-energy state (ZES) is shown by the black solid line. The green solid curves display the fitted function to the first energy levels. Only the six lowest electron and hole energy levels are shown for $-4 \leqslant m \leqslant 4$. The inset of panel (a) shows an enlargement of the energy levels, corresponding to the K valley, around the region where the quantum dot states merge to form the first LL for both IMBC (solid curves) and ZZBC (dashed curves).

symmetry for IMBC, which is apparent from the $\varepsilon^{e}_{\pm 1,m} = -\varepsilon^{h}_{\mp 1,m}$ relationship shown in Fig. 1(a).[6]

Unlike the IMBC, the ZZBC produces the ZES, composed of the $m \leqslant -1$ states in the K valley and $m \geqslant +1$ states in the K' valley (see Sec. II A). Zero-energy states are a trademark feature of infinite structures with bipartite lattices, which have the property of a *global imbalance* in the number of sublattice sites. These states are pseudo-spin-polarized, inhabiting exclusively one sublattice, and are found at exactly zero energy. On the other hand, GQD's possess *local imbalance* in the number of sublattice sites, and should therefore exhibit quasi-zero-energy states, without pseudo-spin-polarization. As a matter of fact, the shift from zero energy occurs due to the hybridization between close sites with a different character of the imbalance.[19] This means that the zigzag edges in real GQD's will be host to quasi-zero-energy states, a properly which is not captured well with the Dirac-Weyl model, since we find a band of states at exactly zero energy in the case of the zigzag boundary condition. This issue will be discussed in more detail in Sec. III, where we use the TB model when calculating the energy spectrum of a circular GQD. For a different geometry that includes both zigzag and armchair edges at the boundaries, e.g., a rectangular graphene flake, the energy spectrum exhibits zero-energy states due to the presence of the zigzag edge. It was shown in Ref. 20 that for the case of a rectangular graphene dot, the number of degenerate zero-energy states depends on the number of armchair atoms.

With increasing magnetic field, the quantum-dot states merge to form the Landau levels (LL's) of graphene. In contrast with semiconductors, the LL's in graphene are nonequidistant and exhibit square-root dependence on the magnetic field.[21] For the IMBC, the first LL ($n = 1$) is composed of $m \leqslant 0$ states, and the higher-energy ($n > 1$) LL's are formed out of $m < n$ states in both the K and K' valleys. Such a behavior is similar to semiconductor QD's.[21] This behavior is also true for the LL's in the K valley of the ZZBC, displayed by the solid lines in Fig. 1(b). The $m \leqslant 0$ states in the K' valley spectrum for the adopted ZZBC and the $m < 0$ states in both valleys for the applied IMBC form the zero-energy ($n = 0$) Landau level (ZLL). We point out that for both IMBC and ZZBC, only one of the valleys contributes to the zeroth Landau level in each band, which is known to be the case in bulk graphene, and is the reason behind the anomalous QHE.[3] For the IMBC, Eqs. (7a) and (7b) do not exhibit a physical solution at zero energy, therefore the quantum dot states that form the ZLL cannot have exactly zero energy in the employed continuum model.

The asymptotic dependence of the energy levels (except for the $n = 0$ state) in both the K and K' valleys for the employed IMBC and large β is given by

$$\varepsilon^{e,h}_{\pm 1,m,n}(\beta) = \pm\sqrt{4\beta\left(n_\rho + \frac{|m| + m}{2}\right)}, \tag{17}$$

where the sign in front accounts for the particle type. For the ZZBC,[22] this relationship also holds for the K valley LL's, whereas the energy level dependence on magnetic field in the K' valley for large β is given by

$$\varepsilon^{e,h}_{-1,m,n}(\beta) = \pm\sqrt{2\beta[2n_\rho + |m| + m - 2\theta(m)]}. \tag{18}$$

Here $n_\rho = 1,2,3,\ldots$ is the radial quantum number, which labels the solutions of Eqs. (15) and (16), and $\theta(m)$ is the Heaviside step function. For $m = 0$, Eq. (18) leads to Eq. (17) for IMBC. Note that each expression in parentheses in Eqs. (17) and (18) is equal to an integer, and therefore has the meaning of the Landau level index n. Furthermore, two different regimes of carrier confinement might be resolved: at low magnetic fields, the confinement is due to graphene termination (i.e., edge confinement). The influence of the edge is suppressed when the magnetic field is large, and the confinement becomes dominated by magnetic field. However, in the continuum model, no matter how large the magnetic field is, it will not suppress the zero-energy band. ZES and its degeneracy will persist throughout the magnetic confinement regime in the ZZBC spectrum, while its wave function is pushed inward toward the center of the dot (see Sec. II A). For both adopted boundary conditions, the transition between the two confinement regimes takes place as the magnetic field increases (see Fig. 1). We may define the transition points between the two regimes as the points where the energies of the states in the quantum dot differ negligibly from the LL energy. These transitions shift toward larger magnetic field with lower m. We should note that the observed dependence of the electron and hole energy levels on magnetic field differs from the one in semiconductor quantum dots, where neither

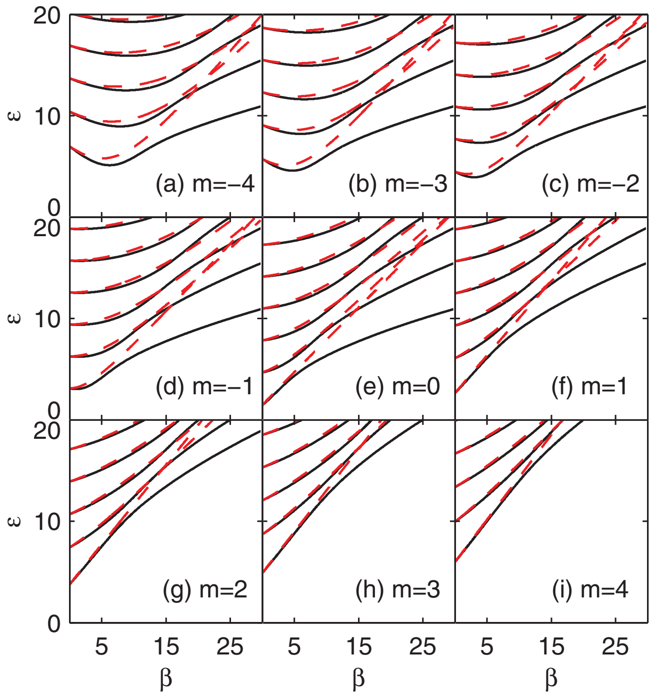

FIG. 2. (Color online) Energy levels of a circular graphene dot as a function of magnetic field, $\beta = eBR^2/2\hbar$ with $R = 70$ nm. The red dashed curves show the approximated spectrum in low magnetic fields, while the exact results are shown by the black solid curves.

ZES nor $n = 0$ LL are found, and the Landau levels increase linearly with β. Moreover, energies of the negative m states obtained from (15) have a tendency to undershoot the positive m energies of the same Landau level, which is not the case for solutions of Eq. (16), as displayed in the inset in Fig. 1(a).

Approximate variations of the electron energy levels with magnetic field, as obtained from first-order perturbation theory (see the Appendix), are displayed in Fig. 2. These energy levels are compared with the exact solutions for the IMBC K valley. Because the applied magnetic field is considered to be a perturbation for the zero-field states, a good agreement between the approximate and exact energy levels is found at low magnetic fields. As a matter of fact, the two approaches start to disagree when the confinement starts to be dominated by the magnetic field. Except for the ZES, similar agreement between the exact calculations and the perturbation theory is found for the states in both valleys when the ZZBC is adopted. Notice that the approximate model cannot describe the states that form the $n = 0$ LL.

E. Angular current

In spite of the major differences in nature of the low-energy quasiparticles, there are some unexpected similarities between semiconductor and graphene quantum dots. One such similarity is the magnetic field dependence of the spatial distribution of the angular current density. The angular current for K valley states is given by

$$j = v_F[\psi^\dagger \sigma_\phi \psi], \tag{19}$$

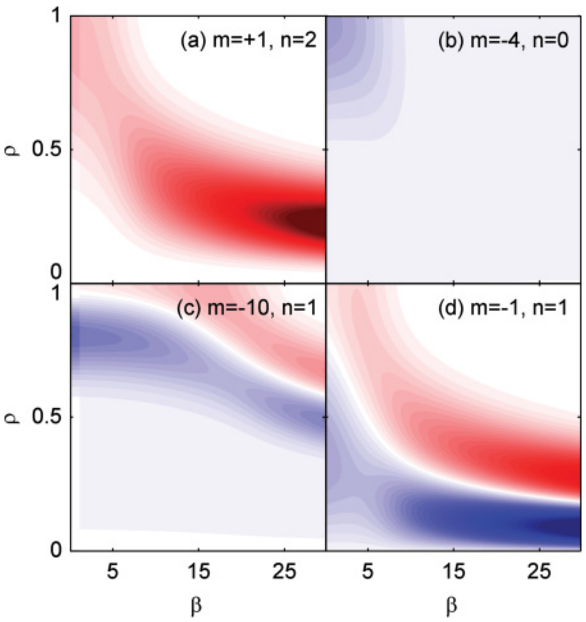

FIG. 3. (Color online) Contour plot of the angular current density for several states vs the normalized magnetic field and the radius. (a) The (+1,2) state, (b) the (−4,0) state, (c) the (−10,1) state, and (d) the (−1,1) state. The counterclockwise and clockwise currents are denoted by red and blue colors, respectively.

where

$$\sigma_\phi = \begin{bmatrix} 0 & -ie^{-i\phi} \\ ie^{i\phi} & 0 \end{bmatrix}. \tag{20}$$

For the K' valley, one has to use the complex conjugate of the previous operator. The final expressions for the angular currents are

$$j_{\phi K} = -2iv_F\chi_1\chi_2, \tag{21a}$$

$$j_{\phi K'} = 2iv_F\chi_1\chi_2. \tag{21b}$$

A density plot of the angular current as a function of magnetic field and radial coordinate is shown in Fig. 3. The ZES exhibits a peculiar property of zero angular current due to its pseudo-spin-polarization. Equation (21b) indeed indicates that if either of the two wave-function components is zero, the current vanishes. The angular currents for the $m = +1, n = 2$; $m = -4, n = 0$; $m = -10, n = 1$; and $m = -1, n = 1$ states are shown in Fig. 3. We show results for the positive m states, the states that form the ZLL, and the $m < 0$ states that form the $n = 1$ LL. The angular currents are shown for the IMBC K valley, but quite similar contour plots are obtained for the IMBC K' valley, and both valleys for the ZZBC. The angular currents for the non-negative m states have the same direction as the current of classical orbits [see Fig. 3(a)]. The internal magnetic field (due to the motion of the electron) is in the opposite direction to the external magnetic field, therefore all non-negative m states exhibit diamagnetic behavior.

Conversely, the state $(m,n) = (-4,0)$, which forms the ZLL, shows weak paramagnetism (small angular current) at low magnetic fields, which diminishes when the magnetic field increases, as displayed in Fig. 3(b). Such a paramagnetic behavior might be explained by edge-skipping orbits close to the edge of the dot that result in a clockwise current. However, as the magnetic field increases, the angular current in the $n = 0$ states vanishes due to the sublattice polarization, as in the ZES. Indeed, a closer look at Eqs. (10) reveals the reason behind it: since $|\psi_2| \sim |\psi_1|/\varepsilon$, shrinking ε will cause the second sublattice wave function to increase in magnitude as compared to the first sublattice wave function. Hence, the ZLL state becomes almost completely localized on the second sublattice with increasing magnetic field, which results in the reduction of the angular current.

The $m < 0$ and $n > 0$ states exhibit a different behavior with increasing magnetic field, as demonstrated in Figs. 3(c) and 3(d) for the $(-10,1)$ and $(-1,1)$ states. Both of these states converge to the $n = 1$ Landau level as β increases. As is depicted, paramagnetic, i.e., clockwise current located mostly close to the edge is the prominent feature of an uncondensed state $(-10,1)$ at low β. On the other hand, the $(-1,1)$ state is energetically closer to the respective Landau level at $\beta = 0$ than $(-10,1)$, which accounts for the larger diamagnetic part of the angular current in this state. As the magnetic field increases, three effects take place: (i) The regions of clockwise current shift toward the ring center, which might be explained as the displacement of the centers of the electron classical orbits inward, i.e., toward the dot center. (ii) Two concentric regions of oppositely oriented angular currents become distinct, i.e., increasing field gives rise to a counterclockwise current on the outer side of the orbits. In fact, the latter property is related to the degree of Landau level condensation of each state, i.e., to the energy difference between the quantum dot state and the Landau level. The lower this difference is, the more pronounced is the diamagnetic component. This is made clear in Fig. 3(d) for the $(-1,1)$ state, which is closer to the first Landau level than $(-10,1)$, and thus has comparatively stronger counterclockwise current. (iii) The region of the counterclockwise current shifts inward too, almost parallel to the region of the clockwise current, as shown in both Figs. 3(c) and 3(d).

In order to describe in more detail how the magnetic field affects the electron localization and the angular currents analyzed above, we show in Fig. 4 contour plots of $|\psi_1|^2$ and $|\psi_2|^2$ in the ρ and β plane for the same states as in Fig. 3. All the states become localized close to the dot center with increasing magnetic field, with the $n = 0$ state resisting the most. Notice that the components of the wave function of the $(+1,2)$ state are comparable to each other over the considered magnetic field range. The latter state has $|\psi|^2$ localized close to the dot edge when the magnetic field is low. For the $(-4,0)$ state, when β increases, ψ_2 starts to dominate, as previously explained, and at high magnetic field ($\beta \approx 10$) it becomes pseudo-spin-polarized, as shown in Figs. 4(c) and 4(d). Notice the transition from a nonpolarized to a polarized pseudospin state, which also highlights the transition from the edge-dominated to the magnetic-field-dominated confinement regime. The eigenfunction representing the nth Landau level in an infinite monolayer graphene sheet, considering the Landau gauge for the vector potential, is given by[23]

$$\langle x,y|\psi\rangle_n = \frac{e^{ik_x x}}{\sqrt{4\pi}} \begin{pmatrix} \pm\langle y|n-1\rangle \\ \langle y|n\rangle \end{pmatrix}, \qquad (22)$$

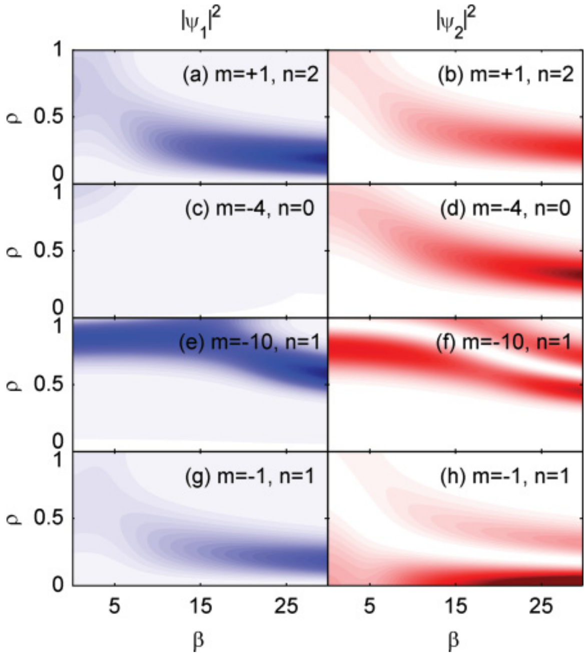

FIG. 4. (Color online) Contour plot of the sublattice contributions for several states vs the normalized magnetic field and the radius. (a) $m = +1, n = 2$ state; (b) $m = -4, n = 0$; (c) $m = -10, n = 1$ state; and (d) $m = -1, n = 1$ state. Red and blue denote electron weights on sublattices 2 and 1, respectively.

where k_x is the wave vector in the x direction and $|n\rangle$ is the nth eigenfunction of the quantum harmonic oscillator in the y direction. For the ZLL ($n = 0$), the upper component is zero and, consequently, this state is fully pseudo-spin-polarized for an infinite graphene sample. In the GQD case, as the magnetic field increases, the lowest energy states, which are not pseudo-spin-polarized in the edge-confinement regime, approach the ZLL and become pseudo-spin-polarized, as expected for this level if no edges are present, i.e., in the regime where the magnetic field confinement dominates. Figures 4(e) and 4(f) show how the wave-function components vary in the $(-10,1)$ state. The spatial localization in this state is less affected by the magnetic field than the localization of the $(-1,1)$ state, which is displayed in Figs. 4(g) and 4(h). However, $|\psi_2|^2(\rho)$ of both the $(-10,1)$ and $(-1,1)$ states have two maxima, which is related to the simultaneous presence of paramagnetic and diamagnetic currents in these states shown in Figs. 3(c) and 3(d).

F. Optical absorption

Optical absorption, for the transition between states i and j, is measured by $|M_{ij}|^2 = |\langle\Psi_i|re^{i\phi_p}|\Psi_j\rangle|^2$, where ϕ_p is formally the polarization angle, having no impact on the final result. Having calculated the matrix elements describing the transition for each possible pair of states, we introduce a Lorentzian-type broadening for the absorption spectrum, and we consider Fermi-Dirac statistics:

$$A_{ij}(E) = \frac{\Gamma_{ij}}{\omega} \frac{[f_{\mathrm{FD}}(\varepsilon_i,\varepsilon_F,T) - f_{\mathrm{FD}}(\varepsilon_j,\varepsilon_F,T)]M_{ij}}{(\varepsilon - \varepsilon_{ij})^2 + \Gamma_{ij}^2}, \qquad (23)$$

where T is the temperature and ω corresponds to the energy of the incident photon ($E = \hbar\omega$). f_{FD} is the Fermi-Dirac distribution and Γ_{ij} is the broadening parameter, which is assumed to be 1 meV in our calculations. The total absorption spectrum is taken to be the sum of all individual transitions $A(E) = \sum_{i,j} A_{i,j}(E)$ for both valleys.

The integral with respect to ϕ in the matrix element M_{ij} is nonzero only when $m_j = m_i$. Furthermore, no selection rule applies to n, which differs from the case of massive graphene, where transitions are allowed only between adjacent Landau levels.[24] Although transitions between states that do not differ by ±1 in the value of n are allowed in the GQD, we found that their contribution to the overall absorption is a few orders of magnitude smaller than the contribution of the $n \rightarrow n \pm 1$ transitions. The matrix elements between the six lowest energy states for m in the range $[-4, +4]$ are taken into account when computing the absorption spectra, which are displayed as contour plots in Fig. 5 for the applied IMBC and two values of temperature, $T = 100$ and 300 K. For each T, the absorption spectra are computed for (dimensionless) Fermi energies $\varepsilon_F = -5$, 0, +5. In all cases displayed in Fig. 5, there exist bright spots around $\varepsilon_{ij} = 3$. They arise from the $n = -2 \rightarrow n = -1$ and $n = 1 \rightarrow n = 2$ transitions, and are appreciable when the Fermi level is either in the conduction or the valence band [Figs. 5(a), 5(b), 5(e), and 5(f)]. Because of the peculiar statistical distribution for $\varepsilon_F = 0$ at temperature as low as $T = 100$ K, the central bright spot disappears from the absorption spectrum, as Fig. 5(c) indicates. However, when T increases to 300 K, the statistical distribution of the initial and final states changes, and the bright spot reappears for $\varepsilon_F = 0$ [see Fig. 5(d)].

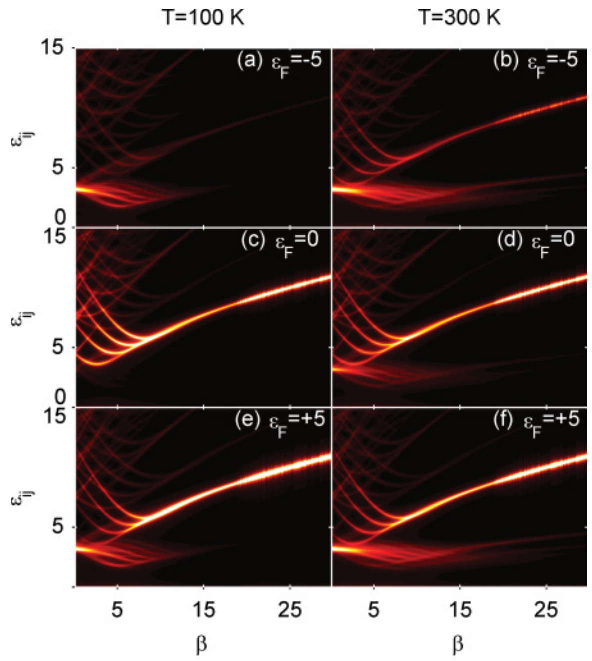

FIG. 5. (Color online) Contour plot of the total absorption spectrum $A(\varepsilon)$ for the IMBC vs magnetic field and transition energy for different values of temperature. Left and right panels correspond, respectively, to temperatures $T = 100$ and 300 K. (a) $\varepsilon_F = -5$, $T = 100$ K; (b) $\varepsilon_F = -5$, $T = 300$ K; (c) $\varepsilon_F = 0$, $T = 100$ K; (d) $\varepsilon_F = 0$, $T = 300$ K; (e) $\varepsilon_F = +5$, $T = 100$ K; and (f) $\varepsilon_F = 5$, $T = 300$ K.

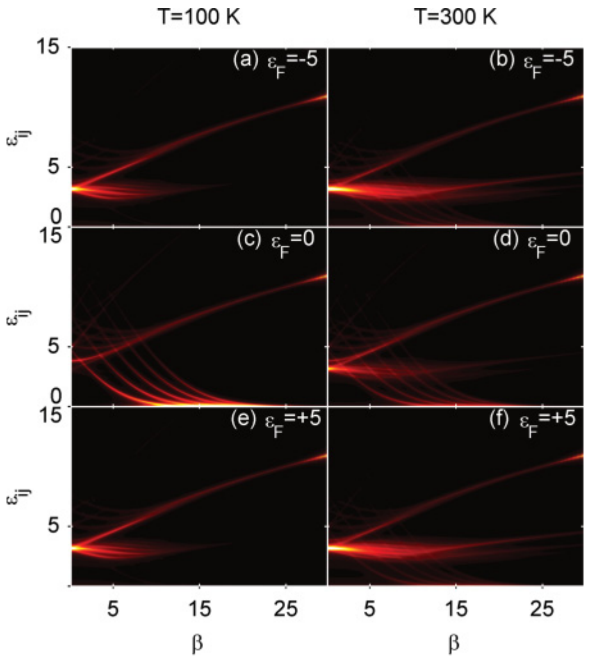

FIG. 6. (Color online) The same as in Fig. 5, but for the ZZBC.

The absorption spectra for the ZZBC shown in Fig. 6 display similar features to the absorption for the IMBC in Fig. 5. In addition to the bright spot, the absorption spectra for both applied boundary conditions exhibit the bright and narrow absorption line that traverses all diagrams in Figs. 5 and 6 nearly diagonally, and it is stronger for the IMBC. This absorption takes place by means of the $n = -1 \rightarrow n = 0$ and $n = 0 \rightarrow n = 1$ transitions in the case of the IMBC. For this case, the energies of the transitions between the states in the two valleys are equal, which favors the appearance of this line. On the other hand, for the adopted ZZBC, the energy spectra of the electron and hole are symmetric within each valley, whereas intervalley electron-hole symmetry is absent. This leads to a less pronounced central absorption peak in the spectrum, which is due to transitions between the ZES and $n = \pm 1$ LL in both valleys. The other noteworthy feature for the ZZBC and $\varepsilon_F = 0$ is the absorption due to interband transitions between the $n = 0$ quantum-dot states in the K' valley, whose transition energy tends to zero when the magnetic field increases.

The absorption spectra for $\varepsilon_F = 0$ and three values of the magnetic field, $\beta = 5$, 10, and 15, are shown in the left and right panel of Fig. 7 for $T = 100$ and 300 K, respectively. The strongest absorption line is due to the $n = -1 \rightarrow n = 0$ and $n = 0 \rightarrow n = 1$ transitions for the IMBC and for transitions between ZES and $n = \pm 1$ LL for the ZZBC. As previously explained, the lack of intervalley electron-hole symmetry for the ZZBC leads to much smaller absorption than for the IMBC. Furthermore, the absorption might increase when the magnetic field increases.

III. THE TIGHT-BINDING MODEL

It is clear that the advantage of using the continuum model lies in the fact that it provides analytical solutions that are easy to handle. However, the continuum model was derived from

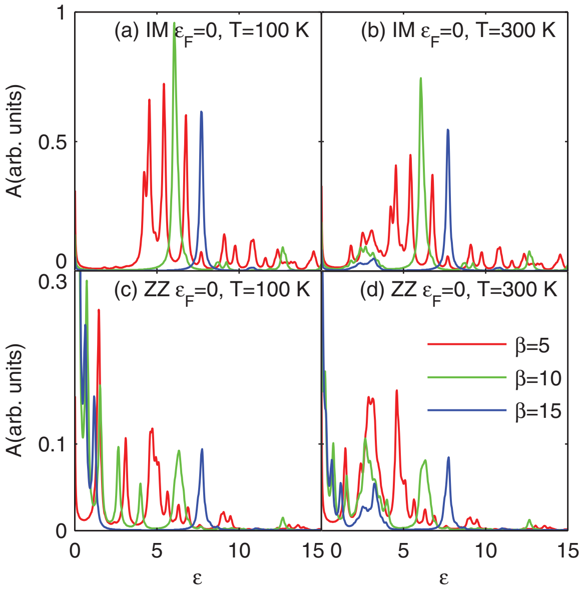

FIG. 7. (Color online) The absorption spectra $A(\varepsilon)$ for $\varepsilon_F = 0$ and two different boundary conditions. Results are shown for $T = 100$ and 300 K, which are displayed in the left and right panels, respectively. (a) The IMBC and $T = 300$ K, (b) the IMBC and $T = 300$ K, (c) the ZZBC and $T = 100$ K, and (d) the ZZBC and $T = 300$ K.

the tight-binding model[2] for an infinite graphene sheet, under the restriction of low-energy charge carriers around the Dirac cones in K and K'. Therefore, it is of interest to investigate the validity range of the continuum model for GQD's.

Actual dot structures are normally cut out from a graphene honeycomb lattice, instead of being surrounded by an infinite-mass media, and therefore cannot have only one type of edge, as illustrated in Fig. 8. However, we intend to demonstrate that the simple boundary conditions described above still provide some agreement with the TB results. The results in this section are obtained from a first-nearest-neighbor tight binding Hamiltonian, which is given by

$$H = \sum_n E_n c_n^\dagger c_n + \sum_{nm} t e^{2\pi i \Phi_{nm}} c_n^\dagger c_m, \qquad (24)$$

where E_n is the on-site energy and c_i ($c_i^\dagger$) is the annihilation (creation) operator, $t = 2.7$ eV is the zero-magnetic-field hopping term, where the C-C distance is $a_0 = 0.142$ nm, $\Phi_{nm} = \frac{1}{\phi_0}\int_{r_n}^{r_m} \boldsymbol{A}\cdot \boldsymbol{dr}$ is the Peierls phase, with $\phi_0 = h/e$ being the magnetic quantum flux, and $\boldsymbol{A} = Bx\hat{\boldsymbol{y}}$ is the vector potential taken in the Landau gauge with perpendicular magnetic field B.

Let us first analyze the case of a circular dot cut out from a graphene lattice, as shown in Fig. 8(a). The energy spectrum in this case is shown in Fig. 9(a) as a function of the magnetic flux through one carbon hexagon $\phi = (3\sqrt{3}a_0^2/2)B$, which looks qualitatively similar to the one shown in Fig. 1(b), for a circular dot with ZZBC within the continuum model. In both cases, groups of states decrease in energy with increasing magnetic field, eventually converging to the Landau levels, and a zero-energy level is observed for any value of magnetic field. On the other hand, some details of the energy spectrum for lower magnetic fields are not captured properly by the continuum model, even for the low-energy levels. For instance, in the results for both the continuum and TB models, the first nonzero level decreases with increasing field whereas the second level starts to increase with the field until it crosses a higher-energy level. However, the anticrossings observed immediately above the described crossing in the TB results are not observed in the continuum model with the ZZBC. The IMBC results in Fig. 1(a) also do not exhibit such anticrossings. Notice this feature is already observed even for the low-energy levels, which are supposed to be within the validity range of the continuum approximation. This can be interpreted as a breakdown of the continuum model.

There is also a surprising feature in this energy spectrum obtained within the TB model: as we zoom in around the zero-energy region, we realize that it is not really a single $E = 0$ curve, but rather a band of curves, as shown in Fig. 10. We considered three different ranges of energy and found curves that exhibit a self-similar-like pattern, which persists until we

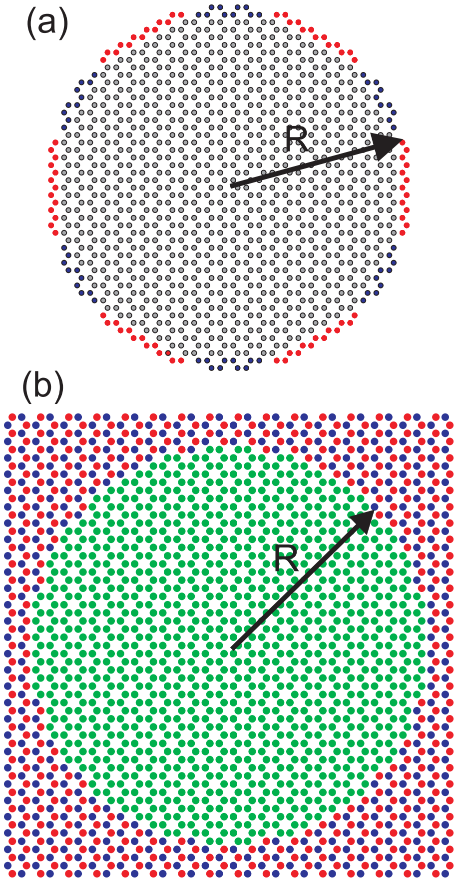

FIG. 8. (Color online) Sketch of the two circular graphene dots of radius R considered in our TB calculations: (a) A circular dot cut out from the graphene honeycomb lattice, where the red (blue) sites refer to zigzag (armchair) boundaries. (b) A circular region (green) surrounded by an infinite-mass media, which is obtained by considering a staggered potential, i.e., a +10 (−10) eV on-site potential for lattice A (B) sites, represented by red (blue) atoms. In both cases, the dot is made out of all the atomic sites that are inside a circle of radius R and that have at least two nearest-neighbor sites inside the circle.

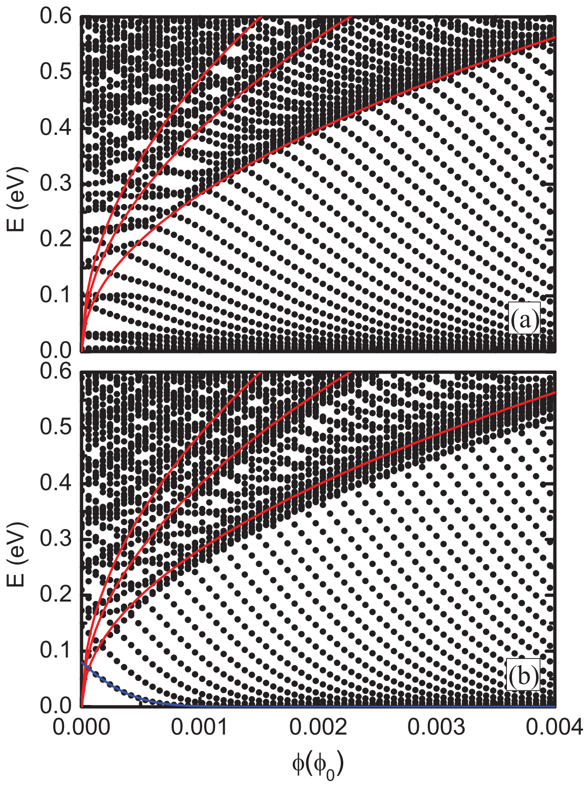

FIG. 9. (Color online) Energy spectrum as a function of the magnetic field, obtained from the TB model for (a) the cut-out graphene dot and (b) the infinite mass defined quantum dot illustrated in Fig. 8 with $R = 10$ nm. The red curves represent the Landau levels in graphene. The blue solid curve in panel (b) shows the fitted function to the first energy level.

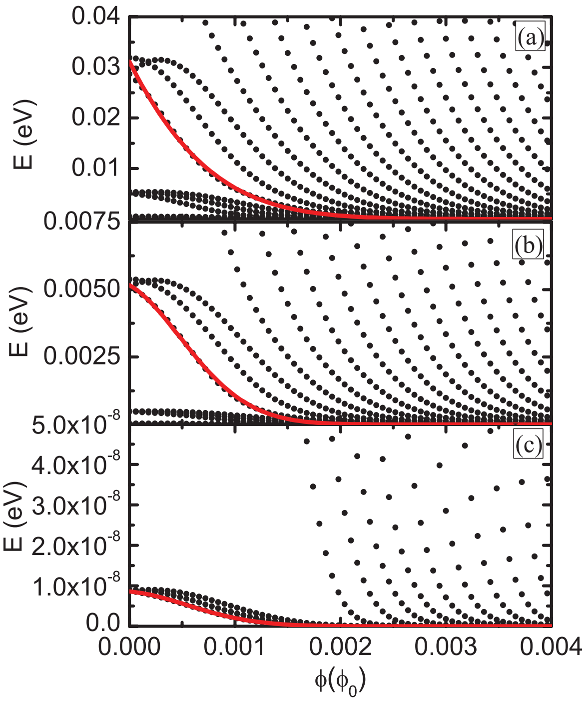

FIG. 10. (Color online) Magnification of the results in Fig. 9(a) for three different energy scales. The red solid curves display the fitted functions to several lowest energy states.

find the lowest energy levels, which are indeed very close to zero ($\approx 10^{-8}$ eV). The results in Figs. 9 and 10 were obtained for $R = 10$ nm. As the dot radius is reduced, similar results are observed but the low-energy states appear farther away from the zero level. For example, for $R = 2$ nm, the lowest level has an energy $E \approx 0.095$ eV, i.e., a 0.190 eV energy gap, even though the dot still exhibits zigzag edge segments. The wave function of these small energy states is localized at the zigzag edges of the circular dot (see Fig. 11). The lowest energy states consist of wave-function pockets localized at the largest width zigzag edge regions [i.e., regions indicated by the red dots in Fig. 8(a)]. Notice, furthermore, that for $B \approx 0$ those low-energy levels are in three groups: (i) the two lowest are degenerate for $B = 0$ and their wave functions are identical up to a rotation of 60°, and (ii) the third level has a slightly larger energy with a wave function consisting of more pockets localized at the edge with a higher rotational symmetry as compared to the previous two. As the magnetic flux increases, the degeneracy of the two lowest levels is lifted in each group and the second state crosses the third (nondegenerate) state at some value of magnetic flux. For higher flux, all these states decrease and end up forming the zeroth Landau level.

Similar to the continuum results, the first energy levels for both IMBC and ZZBC can be fitted to a Gaussian function, i.e., $f(\Phi) = a\exp\{-([\Phi - b]/c)^2\}$, where $(a,b,c)_{\rm IMBC} = (0.16, -0.0006, 0.0007)$ are the fitting parameters for the IMBC [see the blue solid curve in Fig. 9(b)] and $(a,b,c)_{\rm ZZBC} = (0.0008, -11, 92) \times 10^{-5}$ are the fitting parameters for the first energy level with ZZBC [see the red solid curve in Fig. 10(c)]. Notice that the upper energy levels (those decreasing with magnetic field) can also be fitted to a Gaussian function as shown by the red curves in Figs. 10(a) and 10(b) for the ZZBC $[(a,b,c)^{(a)}_{\rm ZZBC} = (0.13, -0.0022, 0.0018)$ and $(a,b,c)^{(b)}_{\rm ZZBC} = (0.0053, -0.00018, 0.0001)$ are the fitting

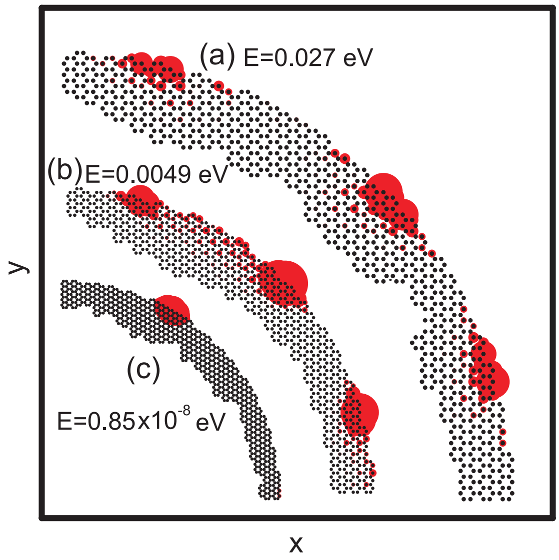

FIG. 11. (Color online) Electron densities corresponding to the energy levels shown by the red solid curves in Fig. 10 for $\Phi/\Phi_0 = 0$. The black dots are the position of the C atoms where we showed only a small strip of the quadrant of the circular graphene flake.

parameters, respectively, for the indicated energy state in Figs. 10(a) and 10(b)].

We now analyze the case of a circular dot surrounded by an infinite-mass media, as illustrated in Fig. 8(b). Although the sublattice symmetry breaking in epitaxial graphene is still a big challenge in order to realize graphene-based electronic devices, recent experiments demonstrated that by choosing the appropriate substrate,[25,26] this can be realized. Such a symmetry breaking is translated into a mass term in the Dirac-Weyl Hamiltonian for graphene. This suggests that a circular graphene dot embedded in an infinite-mass media might be experimentally feasible by means of substrate engineering. Besides, as previously mentioned, an IMBC provides a good description of the magnetization of the edges in a graphene dot. This motivated us to study circular GQD surrounded by a staggered potential, as illustrated in Fig. 8(b). The results obtained by the TB model for such a system are indeed comparable to those from the IMBC in the continuum model: both cases have no zero energy levels, and the anticrossings found for the structure in Fig. 9(a) are not present in the energy spectrum for the infinite-mass confinement in the TB model, which causes it to agree much better with the IMBC results. On the other hand, a broad energy band is found around the Landau levels in the TB results, which is not observed in the continuum model. Nevertheless, this band occurs for high-energy states, which are not expected to be described by the Dirac-Weyl equation, although they follow qualitatively the Landau levels predicted by this equation.

Finally, we investigate how the size of the graphene dot affects their energy spectrum, and we compare the results from the TB and continuum models. Figure 12(a) shows the energy spectrum as a function of the dot radius obtained by the TB model (symbols) for the mass-confinement dot illustrated in Fig. 8(b). The Dirac-Weyl results considering IMBC are shown as red curves, which exhibit very good agreement with the TB results, especially for the lower-energy states and larger dots. Some curves in the TB results do not decay monotonically as $\propto 1/R$; instead, they exhibit a fluctuating behavior, which is more pronounced for smaller radii. Such fluctuations can be linked to the fact that the GQD's studied within the TB model are never perfectly circular, as one can verify in the sketch in Fig. 8(b). In other words, the microscopic details become important as R decreases, and these details cannot be described properly by the analytical model for circular GQD's, based on the continuum approach. For larger dot radii, these edge imperfections are less important, which explains the less pronounced fluctuations in the energy levels as R increases.

The energy spectrum as a function of the radius of the circular dot when cut out from the graphene layer, shown in Fig. 12(b), exhibits the following: (i) even larger fluctuations, (ii) the energies decrease much faster than $1/R$ with increasing R, and (iii) the energy levels are spread out more evenly in the shown energy window. This is due to the fact that, besides the imperfections in the circular shape of the dot, the variations in the number of zigzag and armchair atoms at the edge of the dot also play a role in the energy spectrum as R increases. We notice that as R increases, lower-energy states merge into a very dense $E = 0$ band. This is not expected to be the case in the continuum approximation, where the zero-energy-band states are perfectly degenerate with zero energy even for small radius, and higher-energy states approach zero only for $R \to \infty$. Thus, this feature, along with the self-similarity behavior mentioned earlier, are pure manifestations of the microscopic character of such GQD's, which cannot be described by our IMBC and ZZBC, or by any analytical model within the continuum approach known to date. Indeed, the results obtained by the ZZBC in the continuum model (red curves) give no hint about the energy spectrum, except for the fact that they predict the $1/R$ behavior of some states observed in the TB results. The energy states that decrease much faster than $1/R$ can be fitted to an exponential function, i.e., $E^i = E_0^i e^{-R/R_0^i}$, where E_0^i and R_0^i are fitting parameters and i indicates the eigenstate index. In Fig. 12(b), the five lowest energy levels are shown by the green solid curves, where $E_0^{i=1,2,\ldots,5} = [33.3,17.96,6.24,3.78,3.82]$ eV and $R_0^{i=1,2,\ldots,5} = [0.67,0.87,1.2,1.58,1.84]$ nm. The parameters R_0^i can be related to each other by $R_0^i \approx 1.3 \times R_0^{i-1}$.

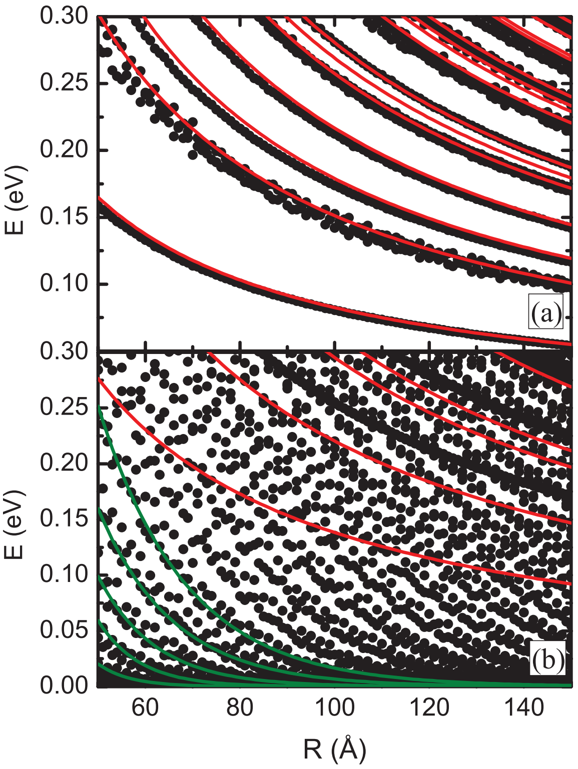

FIG. 12. (Color online) Energy spectrum as a function of the dot radius, in the absence of a magnetic field, obtained from the continuum (red curves) and TB models (symbols), (a) for the infinite mass defined quantum dot illustrated in Fig. 8(b), and (b) for the quantum dot cut out from the graphene layer, illustrated in Fig. 8(a).

IV. CONCLUSION

The electron and hole states in a monolayer graphene circular quantum dot were modeled using the Dirac-Weyl equation. Two distinct types of boundary conditions are employed, namely the infinite-mass and the zigzag boundary conditions. An energy gap near zero energy is only found for the case with an infinite-mass boundary condition, whereas the peculiar zero energy state, which is pseudo-spin-polarized and localized close to the zigzag boundary, exists when the zigzag boundary condition is imposed. An increase of the magnetic field diminishes the influence of the edge on the electron confinement, and the states merge into Landau levels. The obtained spectra exhibit different symmetries between the electron and hole spectra, and also different intervalley symmetries. However, the variation of the angular current density with magnetic field is quite similar for the two adopted boundary conditions.

The states that collapse into the $n = 0$ Landau level (for $B \to \infty$) are found to exhibit paramagnetic behavior due to the influence of the edge, and they become pseudo-spin-polarized when the magnetic field increases. Negative m states are found to exhibit both clockwise and counterclockwise currents when the magnetic field increases. Furthermore, the boundary conditions and the intervalley symmetry are found to influence the absorption spectra. Equal transition energies in the two valleys lead to the most intense absorption line for the adopted infinite-mass boundary condition. On the other hand, different transition energies in the two valleys lead to much smaller absorption oscillator strength if the zigzag boundary condition is used.

Finally, we found that many features of the more realistic TB quantum dots can be described by simplifications made for the circular dots within the continuum approach. Namely, the energy states in the continuum and TB models converge to the LL's at high magnetic field in a similar way. However, due to their inevitable zigzag edges, circular GQD's cut out from a graphene lattice exhibit a dense quasi-zero-energy band, formed by groups of states that exhibit self-similarity. This is a manifestation of the microscopical character of these dots, and can hardly be described by any continuum-based model. Nevertheless, for circular dots based on mass confinement, the TB results and the analytical IMBC results agree very well for lower energies and a larger dot radius. Thus, a secondary conclusion comes from the comparison above: the IMBC for the Dirac-Weyl equation, frequently used to simulate electron states in GQD's, can describe only quantum dots created by mass-related confinement, whereas the actual GQD's cut out from a graphene layer obtained in recent experiments have a much more complex spectrum that, at least in the absence of possible additional potential terms (due to, e.g., edge reconstruction, magnetization, etc.), cannot be described either by IMBC or by ZZBC when using the continuum model.

ACKNOWLEDGMENTS

This work was supported by the EuroGraphene programme of the ESF (project CONGRAN), the Ministry of Education and Science of Serbia, the Belgian Science Policy (IAP), the bilateral projects between Flanders and Brazil, the Flemish Science Foundation (FWO-Vl), and the Brazilian Research Council (CNPq).

APPENDIX: ENERGY LEVELS FOR LOW MAGNETIC FIELDS

We start from Eq. (8) for zero magnetic field, which can be rewritten as

$$D^{(0)}\big|\chi_{1i}^{(0)}\big\rangle = \lambda_i^{(0)}\big|\chi_{1i}^{(0)}\big\rangle, \tag{A1}$$

where the operator $D^{(0)} = -[\frac{d^2}{d\rho^2} + \frac{1}{\rho}\frac{d}{d\rho} - \frac{m^2}{\rho^2}]$, $\lambda_i^{(0)} = (\varepsilon_{\pm 1,m,n}^{e,h,(0)})^2$ (with i being the eigenvalue index), and $|\chi_{1i}^{0}(\rho)\rangle$ is given by Eq. (9). For the case of nonzero magnetic field, we have

$$\big(D^{(0)} + \beta D_1^{(1)} + \beta^2 D_2^{(1)}\big)\big|\chi_{1i}^{(1)}\big\rangle = \lambda_i^{(1)}\big|\chi_{1i}^{(1)}\big\rangle, \tag{A2}$$

where $D_1^{(1)} = 2(m+1)$ and $D_2^{(1)} = \rho^2$. We assume that $|\chi_{1i}^{(1)}\rangle = |\chi_{1i}^{(0)}\rangle$ for small magnetic fields. Multiplying $\langle\chi_{1i}^{(0)}|$ on both sides of the above equation, we have

$$\lambda_i^{(1)} = \lambda_i^{(0)} + 2\beta(m+1) + \beta^2 \frac{\big\langle\chi_{1i}^{(0)}\big|\rho^2\big|\chi_{1i}^{(0)}\big\rangle}{\big\langle\chi_{1i}^{(0)}\big|\chi_{1i}^{(0)}\big\rangle}, \tag{A3}$$

and finally we obtain

$$\varepsilon_{\pm 1,m,n}^{e,h,(1)}(\beta) = \sqrt{\big(\varepsilon_{\pm 1,m,n}^{e,h,(0)}\big)^2 + 2\beta(m+1) + \beta^2 A(m)}, \tag{A4}$$

where

$$A(m) = \frac{\int_0^1 \rho^3 J_m^2\big(\varepsilon_{\pm 1,m,n}^{e,h,(0)}\rho\big)d\rho}{\int_0^1 \rho J_m^2\big(\varepsilon_{\pm 1,m,n}^{e,h,(0)}\rho\big)d\rho} = \frac{m+1}{m+2}\,\frac{{}_2\widetilde{F}_3\big(m+\frac{1}{2}, m+2; m+1, m+3, 2m+1; -\varepsilon_{n,m}^{2(0)}\big)}{{}_2\widetilde{F}_3\big(m+\frac{1}{2}, m+1; m+1, m+2, 2m+1; -\varepsilon_{n,m}^{2(0)}\big)}. \tag{A5}$$

---

[*] marko.grujic@etf.bg.ac.rs
[†] mzarenia@ua.ac.be
[‡] andrey@fisica.ufc.br
[§] milan.tadic@etf.bg.ac.rs
[‖] gil@fisica.ufc.br
[¶] francois.peeters@ua.ac.be

[1] K. S. Novoselov, A. K. Geim, S. V. Morozov, D. Jiang, Y. Zhang, S. V. Dubonos, I. V. Grigorieva, and A. A. Firsov, Science **306**, 666 (2004).

[2] A. H. Castro Neto, F. Guinea, N. M. R. Peres, K. S. Novoselov, and A. K. Geim, Rev. Mod. Phys. **81**, 109 (2009).

[3] M. I. Katsnelson and K. S. Novoselov, Solid State Commun. **143**, 3 (2007).

[4] M. I. Katsnelson, K. S. Novoselov, and A. K. Geim, Nat. Phys. **2**, 620 (2006).

[5] L. A. Ponomarenko, F. Schedin, M. I. Katsnelson, R. Yang, E. W. Hill, K. S. Novoselov, and A. K. Geim, Science **320**, 356 (2008).

[6] S. Schnez, K. Ensslin, M. Sigrist, and T. Ihn, Phys. Rev. B **78**, 195427 (2008).

[7] K. Nakada, M. Fujita, G. Dresselhaus, and M. S. Dresselhaus, Phys. Rev. B **54**, 17954 (1996).

[8] H. P. Heiskanen, M. Manninen, and J. Akola, New J. Phys. **10**, 103015 (2008).

[9] A. V. Rozhkov, G. Giavaras, Y. P. Bliokh, V. Freilikher, and F. Nori, Physics Reports **503**, 77 (2011).

[10] M. Wimmer, A. R. Akhmerov, and F. Guinea, Phys. Rev. B **82**, 045409 (2010).

[11] H. Lee, Y. W. Son, N. Park, S. Han, and J. Yu, Phys. Rev. B **72**, 174431 (2005).

[12] J. Fernández-Rossier and J. J. Palacios, Phys. Rev. Lett. **99**, 177204 (2007).

[13] X. Yan, X. Cui, B. Li, and L. Li, Nano Lett. **10**, 1869 (2010).

[14] Z. Z. Zhang, K. Chang, and F. M. Peeters, Phys Rev B **77**, 235411 (2008).

[15] k is used for ZZBC and τ is used for IMBC, which was done in order to simplify our calculations.

[16] M. V. Berry and R. J. Mondragon, Proc. R. Soc. London, Ser. A **412**, 53 (1987).

[17] D. P. DiVincenzo and E. J. Mele, Phys. Rev. B **29**, 1685 (1984).

[18] A. R. Akhmerov and C. W. J. Beenakker, Phys. Rev. B **77**, 085423 (2008).

[19] J. J. Palacios, J. Fernández-Rossier, and L. Brey, Phys. Rev. B **77**, 195428 (2008).

[20] S. C. Kim, P. S. Park, and S. R. Eric Yang, Phys. Rev. B **81**, 085432 (2010).

[21] C. S. Lent, Phys. Rev. B **43**, 4179 (1991).

[22] Although not presented in the paper, we have also calculated the spectrum stemming from $\psi_2(1,\phi) = 0$. The differences as opposed to the $\psi_1(1,\phi) = 0$ spectrum can be summed up by valley inversion and a shift in angular momentum quantum number, so that $\varepsilon^{\psi_2(1,\phi)=0}_{\pm 1,m} = \varepsilon^{\psi_1(1,\phi)=0}_{\mp 1,m\pm 1}$. This means that the ZLL is found only in the K valley, i.e., $\varepsilon = 0$ states exist only for $mk = +0, +1, +2, \ldots$, etc.

[23] T. M. Rusin and W. Zawadzki, Phys. Rev. B **78**, 125419 (2008).

[24] V. P. Gusynin and S. G. Sharapov, Phys. Rev. B **73**, 245411 (2006).

[25] S. Y. Zhou, G.-H. Gweon, A. V. Fedorov, P. N. First, W. A. de Heer, D.-H. Lee, F. Guinea, A. H. Castro Neto, and A. Lanzara, Nat. Mater. **6**, 770 (2007).

[26] C. R. Dean, A. F. Young, I. Meric, C. Lee, L. Wang, S. Sorgenfrei, K. Watanabe, T. Taniguchi, P. Kim, K. L. Shepard, and J. Hone, Nat. Nanotechnol. **5**, 722 (2010).